

Toward High-Throughput Texturing of Polymer Foils for Enhanced Light Trapping in Flexible Perovskite Solar Cells Using Roll-to-Roll Hot Embossing

Marcos Soldera,* Qiong Wang, Flavio Soldera, Valentin Lang, Antonio Abate, and Andrés Fabián Lasagni

A path to further increase the power conversion efficiency of perovskite solar cells is maximizing sunlight absorption using patterned substrates with enhanced light-trapping capabilities. However, to be competitive with traditional solar cells, especially in niche markets, low-cost texturing methods have to be developed. Herein, a roll-to-roll hot embossing method to pattern flexible polyethylene terephthalate (PET) foils is presented as a proof of concept. The cylindrical mold for the embossing process is structured with periodic grooves by picosecond direct laser interference patterning (DLIP). The optical characterization of the textured PET shows a tenfold increase in the haze factor (diffuse-to-global transmittance ratio) compared with flat PET due to the high-intensity diffracted beams. Flexible triple cation perovskite cells deposited onto these patterned substrates show on average an 8% (relative) higher efficiency than similar devices deposited on a reference flat PET substrate. This enhancement can be attributed to the increase in light trapping provided by the textured substrate. Finally, a cost analysis model shows that the additional cost of integrating the proposed hot embossing step into a perovskite solar module manufacturing facility will represent less than 0.35% of the initial fabrication cost.

sources, and for colored or arbitrary-shaped solar modules for decorative purposes as in building facades.^[1–4] Furthermore, the possibility to fabricate flexible solar modules offers the possibility for integrating the whole manufacturing process into a roll-to-roll (R2R) facility with the potential of reducing dramatically the manufacturing costs.^[5] In this type of process, a flexible substrate, for instance, polymeric or metallic, is sequentially coated with the perovskite and functional thin films using either printing^[6,7] or physical vapor deposition^[8–10] techniques. The process counts also with laser scribing steps to allow the series connection of solar cells and with in-line characterization tools to monitor the whole manufacturing process.^[11–14] In the past years, many advances have been reported toward the R2R fabrication of perovskite-based solar cells and modules.^[15–19]

In the quest for flexible devices with high efficiency, an optimized light management is required to maximize the absorbed sunlight and consequently the power conversion efficiency (PCE). Several approaches have been developed to trap light more efficiently than conventional planar cell designs. For instance, it was recently reported that the efficiency of laboratory-scale perovskite cells can be increased

1. Introduction

Solar cells based on hybrid perovskite absorbers are promising low-cost energy sources for those applications where traditional silicon solar cells cannot compete, for instance, for energy-harvesting semitransparent windows, for flexible wearable power

Dr. M. Soldera, Dr. V. Lang, Prof. A. F. Lasagni
Institut für Fertigungstechnik
Technische Universität Dresden
George-Bähr-Str. 3c, Dresden 01069, Germany
E-mail: marcos.soldera@mailbox.tu-dresden.de

Dr. M. Soldera
PROBIEN, Dto. de Electrotecnia, CONICET
Univ. Nacional del Comahue
Buenos Aires 1400, Neuquén 8300, Argentina

 The ORCID identification number(s) for the author(s) of this article can be found under <https://doi.org/10.1002/adem.201901217>.

© 2020 The Authors. Published by WILEY-VCH Verlag GmbH & Co. KGaA, Weinheim. This is an open access article under the terms of the Creative Commons Attribution License, which permits use, distribution and reproduction in any medium, provided the original work is properly cited.

DOI: 10.1002/adem.201901217

Dr. Q. Wang, Dr. A. Abate
Helmholtz-Zentrum Berlin für Materialien und Energie
Kekuléstraße 5, Berlin 12489, Germany

Dr. F. Soldera
Department Materials Science and Engineering
Saarland University
Campus D3.3, Saarbrücken 66123, Germany

Prof. A. F. Lasagni
Fraunhofer Institute for Material and Beam Technology IWS
Winterbergstraße 28, Dresden 01277, Germany

by integrating diffraction gratings onto the outer side of the substrate^[20] or directly inside the device,^[21–23] using up-/down-converter coatings or nanoparticles,^[24,25] using random microstructures to promote light scattering,^[26,27] and including back electrodes capable of producing plasmonic effects.^[28,29] However, all of them involve multiple time-consuming processing steps and none of them have been produced and tested in R2R facilities yet. Therefore, their feasibility for industrial-scale integration is still an open question.

A convenient path to integrate a simple yet effective light-trapping technique in flexible perovskite solar cells compatible with R2R processing is directly structuring the transparent polymeric substrates by hot embossing in the R2R line. Although this well-established method is suitable for the production of patterned foils at high throughputs as well as providing features with high resolution,^[30–32] the manufacturing of cylindrical molds, or sleeves, is still challenging. Commonly, the sleeves are treated by optical or electron beam lithography, electroplating, nanoimprint lithography, or a combination thereof, implying several manufacturing steps.^[33–36] In contrast to these methods, direct laser interference patterning (DLIP) is a one-step processing technique able to structure seamless sleeves with feature sizes below 1 μm and at processing speeds already reaching 57 $\text{cm}^2 \text{min}^{-1}$.^[37–39] In this method, two or more coherent laser beams are overlapped on the sample surface resulting in a periodic intensity distribution within the interference volume. If the absorbed laser energy is high enough, the material is locally

removed, producing a repetitive surface pattern with a spatial period in the typical range from 500 nm to 10 μm .^[40–42] This technique has already been used to pattern a wide range of complex textures on different materials at throughputs approaching 1 $\text{m}^2 \text{min}^{-1}$ for flat substrates.^[43–49]

The aim of this work is to perform a proof-of-concept study to assess the technical and economic feasibility of increasing the efficiency of state-of-the-art perovskite solar cells using polymeric substrates structured by R2R hot embossing. It is proposed to use DLIP to structure the cylindrical mold, as this technique is easily scalable to industrial production.

2. Results and Discussion

2.1. Patterned Polyethylene Terephthalate Foils

A 300 mm-long nickel sleeve was structured by DLIP using the in-house developed setup shown schematically in **Figure 1a,b**. Three DLIP heads designed for each laser output wavelength, namely 355, 532, and 1064 nm, are mounted on independent linear Z-axes which in turn are installed on a linear X-axis. The light beam is propagated from the laser source by mirrors to the corresponding optical head and then directed to the processing area. The sleeve is mounted on a pneumatic steel cylinder fixed in a rotary axis. This DLIP prototype is designed to structure cylindrical samples with diameters up to 400 mm and lengths up to 1000 mm. The resulting sleeve, shown in **Figure 1c**, was

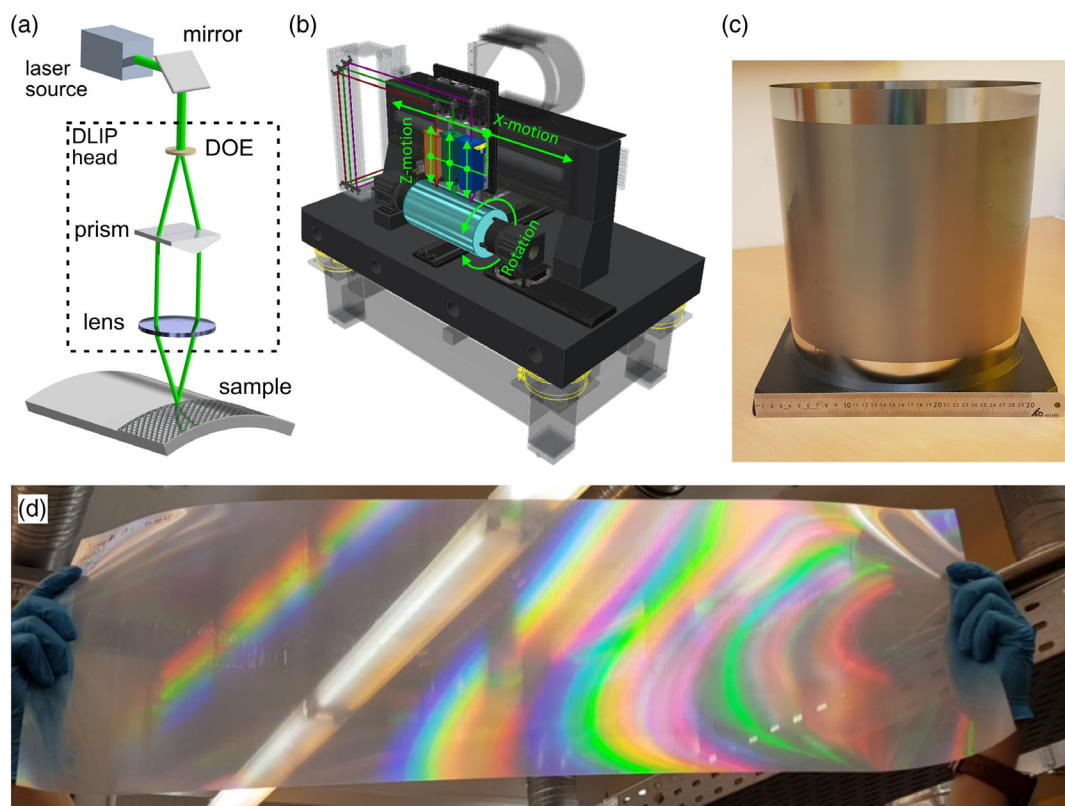


Figure 1. Schematic setups of the a) DLIP optical head and b) DLIP system including three optical heads (one for each laser wavelength) and the rotating sample holder for metallic sleeves. Photographs of c) DLIP-structured nickel sleeve and d) an imprinted PET foil by R2R hot embossing suggest good homogeneity over large areas.

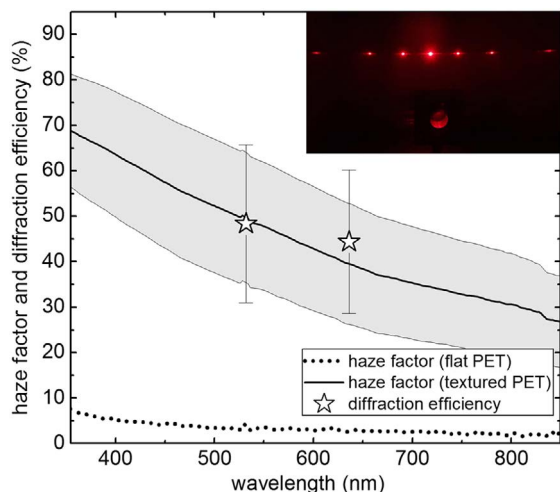


Figure 3. Average haze factor of flat (dotted line) and structured (thick line) PET samples. The gray bands represent the standard deviation of the haze factor in the structured PET. The stars represent the average measured diffraction efficiency (see text for details). The inset shows a photograph of the diffracted beams by the imprinted PET sample.

that a large amount of the incident radiation propagates through angles different from the direct path, which is convenient for enhancing the light-trapping effect in the solar cells. As the imprinted grooves are periodic, the structured PET diffracts light into well-defined angles, as shown in the photograph in the inset of Figure 3. The intensity of the zero, first, and second orders (both positive and negative) at ten different positions of the imprinted PET were recorded (the low intensity of higher orders could not be measured with the used setup) and the diffraction efficiency DE is calculated as follows

$$DE = \frac{\sum_{i \neq 0} I_i}{I_0}, \quad (1)$$

where I_i is the intensity of the diffracted i th order.

In Figure 3, the average DE and its standard deviation are shown with stars at the wavelengths of 532 and 636 nm. Interestingly, the measured DE is close to the average haze factor and enclosed within the standard deviation ranges. Therefore, it can be concluded that although some light scattering is present, most probably due to LIPSS and imprint nonhomogeneities, the dominant mechanism responsible for the high haze factor is diffraction.

2.2. Flexible Perovskite Solar Cells

Perovskite solar cells were deposited onto flat and structured PET foils. The scanning electron microscopy (SEM) images in Figure 4, which were taken at a tilting angle of 52° , represent cross cuts done with Ga-ion milling using a focused ion beam (FIB) in a flat (Figure 4a) and textured (Figure 4b,c) perovskite solar cell. In Figure 4a, the different layers are identified and labeled. In the cross cuts of the textured cell, the periodic line-like structures imprinted on PET with a spatial period of $2.7 \mu\text{m}$ can be recognized. Also, smaller repetitive structures

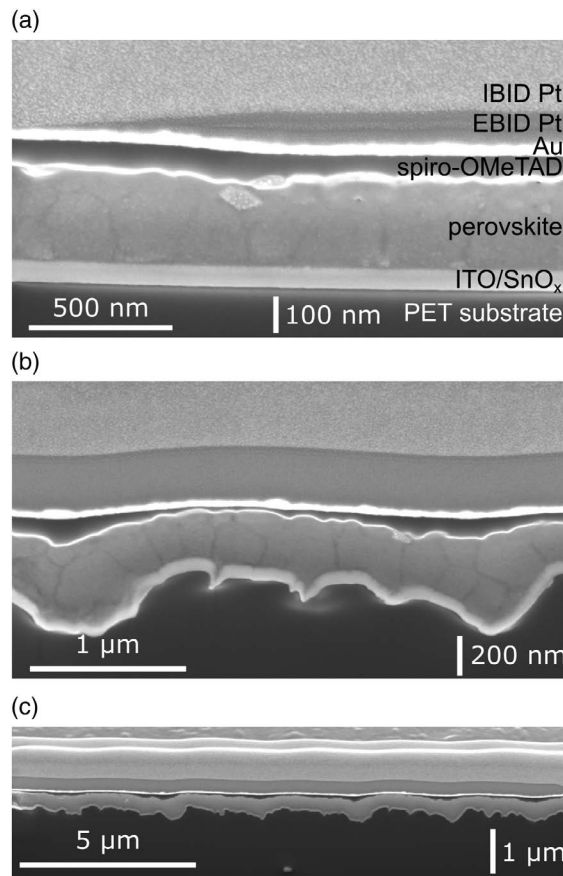


Figure 4. SEM images of cross cuts done with FIB milling of a) flat and b, c) textured perovskite solar cells deposited on PET. Note that the vertical scale bar is corrected for the tilted viewing angle of 52° .

can be identified corresponding to the LSFL, as previously shown in the AFM images of Figure 2. The spatial period of LSFL lies in the range between 400 and 600 nm, whereas their vertical feature size is ≈ 140 nm, in agreement with the AFM measurements. Figure 4b shows clearly that indium tin oxide (ITO) grew conformally on the hierarchically textured PET. While the interface between the perovskite and spiro-OMeTAD still follows the periodicity of the line-like structures, the LIPSS features cannot be distinguished at this interface. It can be observed that despite the spiro-OMeTAD layer having a nonuniform thickness ranging from roughly 30 to 210 nm, shunts between the perovskite and Au are not identified.

The performance of the solar cells was characterized by current–voltage curves and external quantum efficiency (EQE) measurements. Figure 5 shows the output parameters, i.e., a) PCE, b) short-circuit current (J_{sc}), c) open-circuit voltage (V_{oc}), and d) fill factor (FF), measured under simulated AM1.5G illumination of the perovskite solar cells deposited on flexible flat (10 devices) and textured PET (15 devices) as well as on rigid ITO-coated glass (12 devices). Due to the hysteresis present in these types of solar cells, the electrical parameters shown in Figure 5 are determined from the reverse bias cycle (from open-circuit to short-circuit conditions).^[55,56] The open circles are the measured data, whereas the top edge, the middle line, and the bottom edge

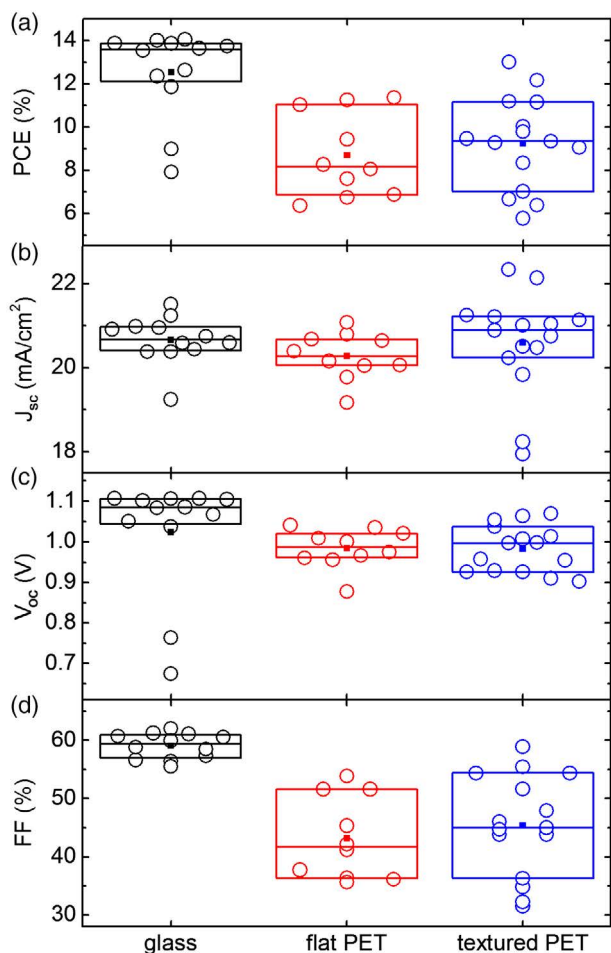


Figure 5. Box chart of photovoltaic parameters, namely a) PCE, b) J_{sc} , c) V_{oc} , and d) FF, of perovskite solar cells deposited on top of glass (black), flat PET (red), and textured PET (blue) substrates.

of the boxes represent the 75%, 50% (or median), and 25% percentiles, respectively, of the corresponding measured output parameter in each substrate type. The solid squares stand for the average value. All the performance parameters in the PET-based devices showed fluctuations within the same processing batch, which can be probably caused by the deviation in the film thickness of the perovskite layer and the top hole transport layer. In addition, the textured samples showed a higher dispersion in all the electrical parameters compared with the flat cells, which can be attributed to inhomogeneous imprinted structures. This could lead to nonuniform layer thicknesses yielding for instance a spread from sample to sample in the light absorption, series resistance, or built-in electric field. As reported in previous studies, these factors can influence significantly all the solar cell performance parameters.^[57–60] On average, the textured solar cells have an efficiency of 9.4%, which is 8% (relative) higher than the average efficiency of the flat cells but still 33% lower than the average efficiency of the glass-based devices. This difference could have originated in the different processing conditions of the glass- and PET-based devices. First, the commercial ITO-coated substrates have a low sheet resistance in contrast to the

sputtered ITO on PET substrates. Although further annealing at 180 °C after sputtering of ITO could help to increase its conductivity,^[61] this thermal process would permanently damage the PET substrate, and it is thus not viable for these cells. Second, the low processing temperature of the perovskite film at 60 °C may result in an increased presence of defects in the perovskite film, which yielded a relatively low open-circuit voltage and FF.

The average short-circuit current and FF are higher in the textured devices compared with those deposited on flat PET by 2% and 4%, respectively, and they explain the higher efficiency in the textured solar cells. The open-circuit voltage is the parameter that shows the lowest dispersion in the three types of solar cells. In this case, there is no significant difference between the average V_{oc} in the flat and textured PET-based solar cells.

Despite the glass-based devices showing the best average output parameters, the best-performing textured solar cell has an efficiency of 13% which is even higher than the average efficiency of 12.5% in the cells deposited on glass.

The current–voltage curves of the best devices deposited on glass, flat, and textured PET are shown in **Figure 6a** and their output parameters are shown in **Table 1**. In the inset of Figure 6, a photograph of the flexible device deposited on structured PET is shown. The key factor that allows a high efficiency in the textured cell is the increased short-circuit current of 22.3 mA cm^{−2}, which is 10% higher than the average J_{sc} of the flat PET devices and 8% higher than that of the glass-based cells.

Figure 6b shows the EQE (left axis) and the integrated short-circuit current calculated from the EQE (right axis), of the best-performing solar cells deposited on glass (black line), flat PET (red line), and textured PET (blue line) substrates. It is shown that for wavelengths shorter than 550 nm, the EQE of the glass-based device is higher than the EQE of the PET-based devices, especially in the ultraviolet (UV) spectrum which is strongly absorbed by the PET substrates. As a consequence, in this spectral range, the integrated J_{sc} is higher for the solar cell deposited on glass than the PET-based devices. In contrast, the cells deposited on PET have a higher EQE for wavelengths longer than 550–600 nm and, particularly, the integrated J_{sc} of the textured device exceeds that of the glass-based cells for wavelengths longer than 655 nm. In the right-most column of Table 1, the integrated J_{sc} in the whole spectral range is listed. Unsurprisingly, the values of J_{sc} obtained directly from the current–voltage curves and calculated from the EQE data do not match, but still both methods show that the textured device delivers the highest J_{sc} , followed by the glass- and flat PET-based devices, respectively. Aside from experimental uncertainties, the mismatch between the J_{sc} values obtained using both methods can be attributed to several factors. For instance, while during the recording of the current–voltage curves, the total device area is illuminated, in the EQE setup, the illuminated area is smaller. This may cause that during the EQE measurement, the dark area acts as a shunting load for the illuminated area draining partially the photocurrent.^[62] Another mismatch factor is the fact that to calculate J_{sc} from EQE data, a standard AM1.5 G spectrum is used, whereas the solar simulator (based on a Xe lamp) used to record the current–voltage curves has a different spectrum.

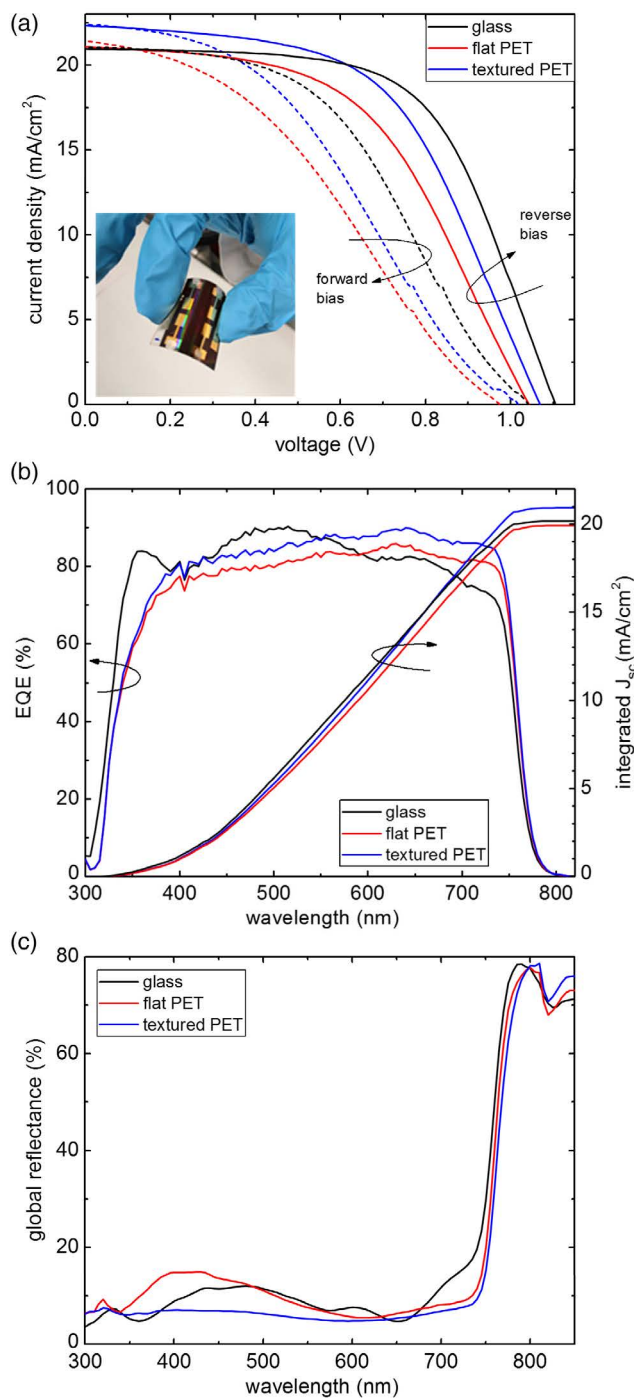


Figure 6. a) Current–voltage curves under illumination, b) EQE measurements and integrated short-circuit current, and c) global reflectance of the best-performing devices deposited on glass and flat and structured PET. The photograph of the inset in (a) shows a flexible perovskite cell deposited on the imprinted PET foil.

When comparing the solar cells fabricated on PET, the EQE of the textured device is higher than the flat cell in the whole spectral range. This enhancement is a clear hint that the patterned substrate enables light trapping inside the cell and increases

Table 1. Electrical output parameters of the best-performing devices deposited on glass and flat and textured PET.

Sample	PCE [%]	J_{sc} [mA cm^{-2}]	V_{oc} [V]	FF [%]	$J_{sc,EQE}$ [mA cm^{-2}] ^{a)}
Glass	14.0	21.0	1.106	60.6	20.2
Flat PET	11.3	21.1	1.044	51.6	19.9
Textured PET	13.0	22.3	1.069	54.4	20.9

^{a)} $J_{sc,EQE}$ is the short-circuit current calculated from the EQE data.

sunlight absorption. Moreover, the global reflectance (see Figure 6c) of the textured device is lower than 7% in the visible spectrum, and it is significantly lower than the reflectance of the flat cells deposited on both PET and glass. The photocurrent loss associated with the reflectance, which is calculated by integrating the standard AM1.5G spectrum modulated by the measured reflectance in the range from 350 to 800 nm, is 4.6 mA cm^{-2} for the glass-based device, 4.3 mA cm^{-2} for the flat PET, and 3.4 mA cm^{-2} for the textured solar cell. The lower reflectance loss observed in the textured solar cell compared with the flat devices explains the $\approx 1 \text{ mA cm}^{-2}$ higher short-circuit current observed in this device.

2.3. Cost Analysis

Considering that, adding the R2R hot embossing step into the solar module production line increases the fabrication costs, a manufacturing cost analysis based on the model developed by Chang et al.^[5] is presented next to evaluate the economic potential of this technology. In that study, five different layer deposition sequences deposited on PET foils are considered, none of which coincide with the cell stack used in this work. Therefore, to keep the following analysis as general as possible, three of those sequences representing middle, high, and low manufacturing cost scenarios are considered. Namely, sequence A has an estimated cost of $65 \text{ U\$ S m}^{-2}$, sequence C has the highest cost of $74 \text{ U\$ S m}^{-2}$, mainly due to the use of the expensive transport layers poly(3-hexylthiophene) (P3HT) and phenyl-C61-butyric acid methyl ester (PCBM), and sequence E has the lowest cost of $37 \text{ U\$ S m}^{-2}$, as cheaper ITO-free electrodes, called “Flextrodes,” are used. Some of the processing steps involved in these sequences require mild annealing steps with temperatures ranging from 60°C to 140°C (see the study by Change et al.^[5] and references therein), which are compatible with PET substrates. For instance, the deposition of the “Flextrode” layer requires an annealing step of 140°C in a hot-air convection oven (size $2 \times 2 \text{ m}^2$) at a web speed of 10 m min^{-1} , implying that the PET foil is exposed locally at this temperature for only 12 s and, therefore, thermal damage in the substrate is prevented.^[63] In turn, for the ITO-based sequences, no additional annealing steps would then be needed after the sputtering of ITO onto the patterned PET foil.^[64,65]

Chang et al. assume multiple R2R lines running simultaneously at a solar module throughput of $4 \text{ m}^2 \text{ h}^{-1}$ in each line to reach a total factory throughput of $830\,000 \text{ m}^2/\text{year}$ (i.e., 0.83 km^2) in a 24/7 operation regime. Considering that the solar module has a width of $\approx 300 \text{ mm}$, this is equivalent

to running each line at a web speed of only 0.07 m min^{-1} , much slower than the value of 4 m min^{-1} used in this work and also much slower than the maximum attainable speed of the used R2R hot embossing unit of 50 m min^{-1} . Thereby it seems reasonable to run a single hot embossing unit at full speed to pattern the PET substrates independently of the solar module production lines, instead of equipping each line with a hot embossing unit. With this assumption, the patterned PET coils can be stocked and then mounted on the perovskite modules R2R lines on demand, which implies that the hot embossing step would not reduce the factory throughput. Even at a moderate web speed of 30 m min^{-1} , operating in a single 8 h shift during 5 days a week and 48 weeks per year, a hot embossing throughput of 1.05 km^2 can be achieved. With these considerations, the manufacturing cost for the hot embossing process is estimated at $0.12 \text{ U}\$\text{ m}^{-2}$, assuming an equipment cost of 300 kU\$, a depreciation time for the equipment of 7 years (as in the study by Chang et al.^[5]), an annual sleeve purchase cost of 5 kU\$, a technician working in the same shift as the unit at a cost of $12.1 \text{ U}\$\text{ h}^{-1}$,^[5] and 100% overhead costs of $50 \text{ kU}\$\text{ year}^{-1}$. Remarkably, the extra cost for the hot embossing unit represents only a tiny fraction of the total manufacturing cost. For instance, for the low-cost sequence E, it represents less than 0.35% of the total cost.

Naturally, the cost per watt peak (Wp) depends on the assumed initial solar module efficiency, the geometric FF (i.e., the actual usable fraction of the module area), as well as the expected PCE increase after the hot embossing patterning step. Figure 7 shows the cost per Wp estimation for the sequences A, C, and E, with a reasonable geometric FF of 68% and assuming a relative efficiency increase of 5%, 10%, and 15%, due to the light-trapping capability of the textured PET. It is shown that the cost reduction correlates almost linearly with the expected relative PCE increase, which is attributed to the practically negligible cost of adding the hot embossing step compared with the total manufacturing cost. For example, considering a solar module fabricated following the sequence A with an initial efficiency of 12%, the cost per Wp can be reduced from $0.64 \text{ U}\$\text{ per Wp}$ to $0.55 \text{ U}\$\text{ per Wp}$ assuming an efficiency enhancement of 15% (relative) after the hot embossing step.

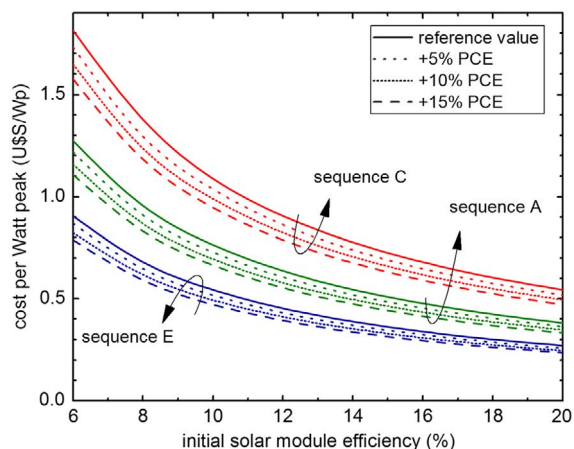


Figure 7. Cost reduction calculation upon incorporating the presented R2R hot embossing method into a perovskite solar cells manufacturing facility, according to the techno-economic model by Chang et al.^[5]

3. Conclusions

In this contribution, a high-throughput and cost-effective method was presented to pattern PET foils with enhanced light-trapping capabilities for flexible perovskite solar cells. Namely, the PET substrates were imprinted by hot embossing in a R2R unit at a web speed of 4 m min^{-1} using a structured nickel sleeve previously patterned by picosecond DLIP. The optical characterization of the imprinted samples revealed a more than tenfold increase in the haze factor compared with the flat substrates, which was mainly attributed to the high intensity of the first- and second-order diffraction peaks. The triple cation perovskite solar cells deposited onto these substrates showed an increase in the short-circuit current and PCE compared with the flat reference cells, due to enhanced light absorption. The maximum achieved efficiency was 13% in the textured cells, which is 15% (relative) higher than the best flat PET-based cell but still 8% (relative) lower than the best cells deposited on commercial ITO-coated glasses. The main difference between the preparation steps of glass and PET-based cells is the low perovskite layer annealing temperature of the PET-based devices imposed by the low thermal resistance of PET. Further studies should be conducted to reduce the defect concentration in the perovskite layer annealed at temperatures lower 70°C . In addition, to address the performance of the flexible solar cells, further electrical characterization over multiple bending cycles should be conducted.

Finally, a cost estimation analysis for perovskite solar modules was adapted including the proposed hot embossing step, showing that the associated additional costs are negligible compared with the module manufacturing cost.

4. Experimental Section

Materials: A nickel sleeve with a thickness of $200 \mu\text{m}$, a width of 300 mm , and a diameter of 300 mm (Saechsische Walzengravur GmbH, Germany) was structured by DLIP. The sleeve initial surface roughness (S_a) was 61 nm . Before and after the laser process, the sleeve was cleaned using isopropanol. No additional coatings, such as antisticking layers, were applied to the sleeve before or after the laser treatment.

For the hot embossing process, a $200 \mu\text{m}$ -thick and 250 mm -wide glycol-modified polyethylene terephthalate (PET-GAG) foil (Pütz Folien GmbH + Co. KG, Germany) was used as the substrate. According to the manufacturer, the PET Vicat softening point was 71°C .

Sleeve Structuring by Direct Laser Interference Patterning: An in-house DLIP (developed by Fraunhofer IWS—TU Dresden) setup equipped with a picosecond-pulsed solid-state laser (Edgewave PX200, Germany) with an output power of 10 W was used to pattern the Ni sleeve. The laser operated at a wavelength of 1064 nm , a pulse duration of 10 ps , a repetition rate of 10 kHz , and a fluence on the sample of 2.2 J cm^{-2} . The optical head is described schematically, as shown in Figure 1a, and it consisted of a diffractive optical element (DOE) to split the primary laser beam into two sub-beams which were parallelized by prism and then focused on the sample by a lens. The sleeve was mounted on a rotary axis system, as shown in Figure 1b. Adjusting the overlapping beams angle by varying the distance between the prism and DOE, line-like structures with a spatial period of $2.7 \mu\text{m}$ were fabricated. A pulse-to-pulse feed of $10 \mu\text{m}$ and a hatch distance of $100 \mu\text{m}$ were set.

PET Patterning by R2R Hot Embossing: The used R2R hot embossing system (R2R Basecoater BC51, Coatema Coating Machinery GmbH, Germany) allowed web speeds from 1 to 50 m min^{-1} implying a maximum throughput of $12.5 \text{ m}^2 \text{ min}^{-1}$. The temperature of the top roller was held at

75 °C, slightly above the Vicat softening point of PET to avoid sticking to the structured sleeve. The bottom roller was left at room temperature. The web speed was set at 4 m min⁻¹.

Direct and Global Transmittance: A spectrophotometer (Shimadzu SolidSpec-3700, Germany) equipped with an integrating sphere was used for measuring the diffuse and direct transmittance in the wavelength range from 350 to 800 nm. The measurements were repeated in ten different positions on the structured PET samples.

Diffraction Efficiency: To measure the diffraction efficiency of the structured PET, the samples were illuminated with green (532 nm) and red (636 nm) lasers and the transmitted intensities of the zero, first, and second diffraction orders were measured using an optical powermeter (ThorLabs PM100D, Germany). Ten measurements at different sample positions were carried out for each used laser.

Morphological Characterization: The topography of the structured PET foils was measured with an atomic force microscope CoreAFM (Nanosurf AG, Switzerland) in the tapping mode. SEM images were taken using a FIB/SEM dual beam system (FEI Helios 600, Thermo Fisher Scientific, USA) at an acceleration voltage of 5 kV. Cross sections of the solar cells were done with a FIB using Ga ions at an acceleration voltage of 30 kV. To prevent damage from Ga-ion imaging or milling, the regions of interest were previously coated with a 100–500 nm-thick Pt layer deposited by electron beam-induced deposition (EBID). On top of this layer, a second thicker Pt layer with a thickness between 1 and 2 μm was deposited by ion beam-induced deposition (IBID), improving the damage resistance and allowing the preparation of homogeneous cross sections.

Perovskite Solar Cells Preparation: Prepatterned ITO-coated glass substrates were purchased from Automatic Research GmbH (Germany). The substrates were sequentially cleaned in soap water, acetone, and isopropanol for 15 min, respectively. Before the deposition of tin oxide, the substrates were further processed by a UV–ozone treatment of 15 min.

PET substrates were cleaned with isopropanol for 10 min, and then they were blown dry before the sputtering of ITO (100 nm). The substrates were then transferred to the chamber for the atomic layer deposition (ALD) of tin oxide using an Arradiance GEMStar (USA) reactor. Approximately 7 nm ALD tin oxide was deposited using Tetrakis(dimethylamino)tin(IV) (TDMASn) as the precursor, at a temperature of 60 °C with a growth rate of 0.17 nm per cycle for 41 cycles.

Triple-cation perovskite was prepared and deposited as described in the study by Wang et al.^[66] Here, the annealing temperature was 60 °C for PET substrates and 100 °C for ITO-coated glass substrates. Spiro-OMeTAD solution was prepared following the study by Wang et al.^[66] Au thin film with a thickness of ≈80 nm was thermally evaporated as the top electrode. All the devices had an active area of 0.16 cm².

Device Characterization: The cells were illuminated with a standard AM1.5G 100 mW cm⁻² spectrum using a Wavelabs Sinus-70 LED class AAA solar simulator. The light intensity was calibrated with a silicon reference cell measured at Fraunhofer ISE. The current–voltage (*JV*) curves of perovskite solar cells were measured using a Keithley 2400 SMU with a voltage step of 10 mV, an integration time of 50 ms per point, and settling time of 50 ms after setting the bias level. The obtained scan rate was 100 mV s⁻¹. The EQE spectra were measured using an Oriel Instruments QEPVSI-b (USA) system integrated with a Newport 300 W (USA) xenon arc lamp. Monochromatic light was obtained using a Newport Cornerstone 260 (USA) monochromator and chopped at a frequency of 78 Hz. Using optical fibers, the light was directed to the device surface. Before recording the EQE, the spectrum distribution of the setup was calibrated using a Si reference cell with known spectral response.

Device Reflectance: The reflection of full devices was measured using a PerkinElmer Lambda 1050 UV/VIS/NIR spectrophotometer (USA) with an integrating sphere.

Acknowledgements

M.S. acknowledges the Alexander von Humboldt Foundation for supporting this work. The authors would like to thank Yuan Liu (IAPP, TU Dresden) for the assistance with global transmittance measurements.

This project was funded by the European Regional Development Fund (ERDF) and cofinanced under taxation on the basis of the budget adopted by the members of the Saxon State Parliament. A.A. acknowledges the financial support from the National Natural Science Foundation of China (project no. 21750110442).

Conflict of Interest

The authors declare no conflict of interest.

Keywords

direct laser interference patterning, flexible optoelectronics, light trapping, perovskite solar cells, roll-to-roll hot embossing

Received: October 9, 2019

Revised: November 18, 2019

Published online: January 9, 2020

- [1] C. J. Traverse, R. Pandey, M. C. Barr, R. R. Lunt, *Nat. Energy* **2017**, *2*, 849.
- [2] K.-T. Lee, M. Fukuda, S. Joglekar, L. Jay Guo, *J. Mater. Chem. C* **2015**, *3*, 5377.
- [3] B. Jo Kim, D. Hoe Kim, Y.-Y. Lee, H.-W. Shin, G. Sang Han, J. Sug Hong, K. Mahmood, T. Kyu Ahn, Y.-C. Joo, K. Sun Hong, N.-G. Park, S. Lee, H. Suk Jung, *Energy Environ. Sci.* **2015**, *8*, 916.
- [4] J.-Y. Lam, J.-Y. Chen, P.-C. Tsai, Y.-T. Hsieh, C.-C. Chueh, S.-H. Tung, W.-C. Chen, *RSC Adv.* **2017**, *7*, 54361.
- [5] N. L. Chang, A. W. Y. Ho-Baillie, D. Vak, M. Gao, M. A. Green, R. J. Egan, *Sol. Energy Mater. Sol. Cells* **2018**, *174*, 314.
- [6] Z. Li, T. R. Klein, D. H. Kim, M. Yang, J. J. Berry, M. F. A. M. van Hest, K. Zhu, *Nat. Rev. Mater.* **2018**, *3*, 18017.
- [7] D. Angmo, T. T. Larsen-Olsen, M. Jørgensen, R. R. Søndergaard, F. C. Krebs, *Adv. Energy Mater.* **2013**, *3*, 172.
- [8] J.-I. Park, J. H. Heo, S.-H. Park, K. I. Hong, H. G. Jeong, S. H. Im, H.-K. Kim, *J. Power Sources* **2017**, *341*, 340.
- [9] K.-H. Choi, J.-A. Jeong, J.-W. Kang, D.-G. Kim, J. K. Kim, S.-I. Na, D.-Y. Kim, S.-S. Kim, H.-K. Kim, *Sol. Energy Mater. Sol. Cells* **2009**, *93*, 1248.
- [10] D. Kaduwal, H.-F. Schlieiermacher, J. Schulz-Gericke, T. Kroyer, B. Zimmermann, U. Würfel, *Sol. Energy Mater. Sol. Cells* **2014**, *124*, 92.
- [11] G. Mincuzzi, A. L. Palma, A. Di Carlo, T. M. Brown, *ChemElectroChem* **2016**, *3*, 9.
- [12] M. Yang, D. H. Kim, T. R. Klein, Z. Li, M. O. Reese, B. J. Tremolet de Villers, J. J. Berry, M. F. A. M. van Hest, K. Zhu, *ACS Energy Lett.* **2018**, *3*, 322.
- [13] S. Logothetidis, D. Georgiou, A. Laskarakis, C. Koidis, N. Kalfagiannis, *Sol. Energy Mater. Sol. Cells* **2013**, *112*, 144.
- [14] M. V. Madsen, K. O. Sylvester-Hvid, B. Dastmalchi, K. Hingerl, K. Norrman, T. Tromholt, M. Manceau, D. Angmo, F. C. Krebs, *J. Phys. Chem. C* **2011**, *115*, 10817.
- [15] K. Hwang, Y.-S. Jung, Y.-J. Heo, F. H. Scholes, S. E. Watkins, J. Subbiah, D. J. Jones, D.-Y. Kim, D. Vak, *Adv. Mater.* **2015**, *27*, 1241.
- [16] T. M. Schmidt, T. T. Larsen-Olsen, J. E. Carlé, D. Angmo, F. C. Krebs, *Adv. Energy Mater.* **2015**, *5*, 1500569.
- [17] Z. Gu, L. Zuo, T. T. Larsen-Olsen, T. Ye, G. Wu, F. C. Krebs, H. Chen, *J. Mater. Chem. C* **2015**, *3*, 24254.
- [18] Y. Galagan, F. D. Giacomo, H. Gorter, G. Kirchner, I. de Vries, R. Andriessen, P. Groen, *Adv. Energy Mater.* **2018**, *8*, 1801935.
- [19] J.-E. Kim, S.-S. Kim, C. Zuo, M. Gao, D. Vak, D.-Y. Kim, *Adv. Funct. Mater.* **2019**, *29*, 1809194.

- [20] M. M. Tavakoli, K.-H. Tsui, Q. Zhang, J. He, Y. Yao, D. Li, Z. Fan, *ACS Nano* **2015**, *9*, 10287.
- [21] J. Wei, R.-P. Xu, Y.-Q. Li, C. Li, J.-D. Chen, X.-D. Zhao, Z.-Z. Xie, C.-S. Lee, W.-J. Zhang, J.-X. Tang, *Adv. Energy Mater.* **2017**, *7*, 1700492.
- [22] Y. Wang, P. Wang, X. Zhou, C. Li, H. Li, X. Hu, F. Li, X. Liu, M. Li, Y. Song, *Adv. Energy Mater.* **2018**, *8*, 1702960.
- [23] U. W. Paetzold, W. Qiu, F. Finger, J. Poortmans, D. Cheyns, *Appl. Phys. Lett.* **2015**, *106*, 173101.
- [24] F.-L. Meng, J.-J. Wu, E.-F. Zhao, Y.-Z. Zheng, M.-L. Huang, L.-M. Dai, X. Tao, J.-F. Chen, *Nanoscale* **2017**, *9*, 18535.
- [25] L. Jiang, W. Chen, J. Zheng, L. Zhu, L. Mo, Z. Li, L. Hu, T. Hayat, A. Alsaedi, C. Zhang, S. Dai, *ACS Appl. Mater. Interfaces* **2017**, *9*, 26958.
- [26] M. Jošt, S. Albrecht, L. Kegelmann, C. M. Wolff, F. Lang, B. Lipovšek, J. Krč, L. Korte, D. Neher, B. Rech, *ACS Photonics* **2017**, *4*, 1232.
- [27] F. Wang, Y. Zhang, M. Yang, L. Fan, L. Yang, Y. Sui, J. Yang, X. Zhang, *Nano Energy* **2019**, *60*, 198.
- [28] M. Saliba, W. Zhang, V. M. Burlakov, S. D. Stranks, Y. Sun, J. M. Ball, M. B. Johnston, A. Goriely, U. Wiesner, H. J. Snaith, *Adv. Funct. Mater.* **2015**, *25*, 5038.
- [29] M. Long, Z. Chen, T. Zhang, Y. Xiao, X. Zeng, J. Chen, K. Yan, J. Xu, *Nanoscale* **2016**, *8*, 6290.
- [30] S. H. Ahn, L. J. Guo, *Adv. Mater.* **2008**, *20*, 2044.
- [31] T. Velten, F. Bauerfeld, H. Schuck, S. Scherbaum, C. Landesberger, K. Bock, *Microsyst. Technol.* **2011**, *17*, 619.
- [32] Y. Deng, P. Yi, L. Peng, X. Lai, Z. Lin, *J. Micromech. Microeng.* **2014**, *24*, 045023.
- [33] A. Striegel, M. Schneider, N. Schneider, C. Benkel, M. Worgull, *Microelectron. Eng.* **2018**, *194*, 8.
- [34] A. Habermehl, P. Brenner, R. Huber, A. Mertens, F. Winkler, L. Hahn, M. Guttmann, C. Eschenbaum, U. Lemmer, *Adv. Eng. Mater.* **2019**, *21*, 1900110.
- [35] L. Peng, H. Wu, Y. Shu, P. Yi, Y. Deng, X. Lai, *Rev. Sci. Instrum.* **2016**, *87*, 105120.
- [36] S. H. Ahn, L. J. Guo, *ACS Nano* **2009**, *3*, 2304.
- [37] A. Rank, V. Lang, A. F. Lasagni, *Adv. Eng. Mater.* **2017**, *19*, 1700201.
- [38] V. Lang, A. Rank, A. F. Lasagni, *Adv. Eng. Mater.* **2017**, *19*, 1700126.
- [39] A. Rank, V. Lang, B. Voisiat, A. F. Lasagni, in *Laser-Based Micro- and Nanoprocessing XIII*, International Society For Optics And Photonics, San Francisco, USA **2019**, p. 109060V.
- [40] M. Bieda, M. Siebold, A. F. Lasagni, *Appl. Surf. Sci.* **2016**, *387*, 175.
- [41] A. F. Lasagni, M. Bieda, T. Roch, D. Langheinrich, *Laser Tech. J.* **2011**, *8*, 45.
- [42] S. Alamri, A. F. Lasagni, *Opt. Express* **2017**, *25*, 9603.
- [43] M. Hans, F. Müller, S. Grandthyll, S. Hüfner, F. Mücklich, *Appl. Surf. Sci.* **2012**, *263*, 416.
- [44] T. Tavera, N. Pérez, A. Rodríguez, P. Yurrita, S. M. Olaizola, E. Castaño, *Appl. Surf. Sci.* **2011**, *258*, 1175.
- [45] V. Lang, T. Roch, A. F. Lasagni, in *Laser-Based Micro- and Nanoprocessing XIII*, Society for Optics and Photonics, San Francisco, USA **2016**, pp. 1–8.
- [46] S. Alamri, A. I. Aguilar-Morales, A. F. Lasagni, *Eur. Polym. J.* **2018**, *99*, 27.
- [47] S. Indrišūnas, B. Voisiat, M. Gedvilas, G. Račiukaitis, *J. Laser. Appl.* **2017**, *29*, 011501.
- [48] M. R. S. Castro, A. F. Lasagni, H. K. Schmidt, F. Mücklich, *Appl. Surf. Sci.* **2008**, *254*, 5874.
- [49] S. Fang, L. Llanes, S. Klein, C. Gachot, A. Rosenkranz, D. Bähre, F. Mücklich, in *IOP Conference Series: Materials Science and Engineering*, IOP Publishing, Bristol, England **2017**, Vol. 258, p. 012006.
- [50] P. Gregorčič, M. Sedlaček, B. Podgornik, J. Reif, *Appl. Surf. Sci.* **2016**, *387*, 698.
- [51] J. Bonse, J. Krüger, S. Höhm, A. Rosenfeld, *J. Laser Appl.* **2012**, *24*, 042006.
- [52] J. V. Obona, V. Ocelík, J. Z. Skolski, V. S. Mitko, G. R. Römer, A. J. Huis, J. T. De Hosson, *Appl. Surf. Sci.* **2011**, *258*, 1555.
- [53] G. R. Römer, A. J. Huis, J. Meijer, M. N. Groenendijk, *CIRP Ann.* **2009**, *58*, 201.
- [54] S. Fay, J. Steinhauser, N. Oliveira, E. Vallat-Sauvain, C. Ballif, *Thin Solid Films* **2007**, *515*, 8558.
- [55] H. J. Snaith, A. Abate, J. M. Ball, G. E. Eperon, T. Leijtens, N. K. Noel, S. D. Stranks, J. T.-W. Wang, K. Wojciechowski, W. Zhang, *J. Phys. Chem. Lett.* **2014**, *5*, 1511.
- [56] Q. Wang, N. Phung, D. D. Girolamo, P. Vivo, A. Abate, *Energy Environ. Sci.* **2019**, *12*, 865.
- [57] Q. Lin, A. Armin, R. C. R. Nagiri, P. L. Burn, P. Meredith, *Nat. Photonics* **2015**, *9*, 106.
- [58] K. Taretto, M. Soldera, A. Koffman-Frischknecht, *IEEE J. Photovoltaics* **2017**, *7*, 206.
- [59] D. Liu, M. K. Gangishetty, T. L. Kelly, *J. Mater. Chem. A* **2014**, *2*, 19873.
- [60] M. Saliba, J.-P. Correa-Baena, C. M. Wolff, M. Stollerfoht, N. Phung, S. Albrecht, D. Neher, A. Abate, *Chem. Mater.* **2018**, *30*, 4193.
- [61] D. Zhang, A. Tavakoliyarakhi, Y. Wu, R. A. C. M. M. van Swaaij, M. Zeman, *Energy Proc.* **2011**, *8*, 207.
- [62] R. Scheer, H.W. Schock, *Chalcogenide Photovoltaics: Physics, Technologies, and Thin Film Devices*, Wiley-VCH, Weinheim, Germany **2011**, p. 311.
- [63] M. Hösel, R. R. Søndergaard, M. Jørgensen, F. C. Krebs, *Energy Technol.* **2013**, *1*, 102.
- [64] S.-H. Park, S.-J. Lee, J. H. Lee, J. Kal, J. Hahn, H.-K. Kim, *Org. Electron.* **2016**, *30*, 112.
- [65] H.-K. Kim, J.-A. Jeong, K.-H. Choi, S.-W. Jeong, J.-W. Kang, *Electrochem. Solid-State Lett.* **2009**, *12*, H169.
- [66] Q. Wang, E. Mosconi, C. Wolff, J. Li, D. Neher, F. D. Angelis, G. P. Suranna, R. Grisorio, A. Abate, *Adv. Energy Mater.* **2019**, *9*, 1900990.